2023 IEEE Symposium on Electromagnetic Compatibility & Signal/Power Integrity (EMC+SIPI) | 979-8-3503-0976-8/23/$31.00 ©2023 IEEE | DOI: 10.1109/EMCSIPI50001.2023.10241427

On the Permittivity of XT-CF20

Aaron Harmon
Dept. of Electrical and Computer Engineering – Electromagnetic Compatibility Laboratory
Missouri University of Science and Technology
Rolla, MO, USA
afhpq4@umsystem.edu

Wei Zhang
Dept. of Electrical and Computer Engineering – Electromagnetic Compatibility Laboratory
Missouri University of Science and Technology
Rolla, MO, USA
wznkm@umsystem.edu

Dr. Victor Khilkevich
Dept. of Electrical and Computer Engineering – Electromagnetic Compatibility Laboratory
Missouri University of Science and Technology
Rolla, MO, USA
khilkevichv@umsystem.edu

***Abstract*—In this work, the permittivity of a 3D-printed carbon fiber-loaded anisotropic material, XT-CF20, is examined further. The microstructure of XT-CF20 is first examined via optical imaging and is shown to be composed of inclusions that are aligned with the print direction of the sample. The permittivity tensor for the aligned microstructure is then measured using a capacitive measurement technique and simulations are provided to demonstrate the validity of this measurement method. The simulated permittivity values for XT-CF20 samples with varying infill structures are then presented and compared to the measured permittivity values of said samples. An error of less than 12% between the simulated and measured permittivity values was observed validating the measured permittivity tensor and claims about the cause of the anisotropy presented in this work. The pronounced effect of a sample's infill on the permittivity tensor of the sample is then discussed along with the conclusions of this work and possible future topics of work for the authors.**

Keywords—Anisotropy, Composite Dielectric, High Permittivity Dielectric, Macrostructure, Microstructure, Permittivity, 3D Printing.

I. INTRODUCTION

By doping a base material with inclusions of another material one can modulate its properties. The most commonly modulated properties are the electrical, optical, and structural ones however other properties like thermal conductivity, chemical resistance, viscosity, etc. can also be modulated using the correct dopant [1 – 3]. Doping is now becoming more prevalent in the 3D printing industry as many doped filaments are commercially available for printing. For instance, [4 – 6] are all examples of Polylactic Acid (PLA) base filaments that have been doped to have either enhanced electrical, optical, and or structural properties.

A particularly interesting doped filament is ColorFabb XT-CF20 (CF20) [7]. CF20 is a co-Polyester filament doped with chopped carbon fibers for added strength and wear resistance. While these fibers do increase the strength and wear resistance of CF20, they also strongly modulate the permittivity of CF20 resulting in a high permittivity composite dielectric. This makes CF20 an interesting material for high-frequency applications because devices such as antennas, polarizers, and absorbers, [8 – 10], can all take advantage of a high permittivity dielectric material. A notable example of this for the electromagnetic compatibility (EMC) domain is presented in [11] where a super thin wave absorber was created from a high permittivity graphite loaded ethylene propylene diene methylene (EPDM) rubber. This absorber provided more than 20 dB of absorption at 2 GHz and illustrates how high permittivity dielectrics can be used in the EMC domain.

The permittivity of a CF20 sample was previously investigated by the authors in [12]. In this investigation, the permittivity tensor of a CF20 sample, printed with an orthogonal rectilinear infill pattern, was reported to be $\epsilon_{r,xyz}$ = (21.2, 19.6, 6.8) in the range from 1 MHz to 18 GHz. While [12] clearly illustrated the high permittivity anisotropic nature of the CF20 dielectric, it did not comment on the underlying cause of this anisotropy nor explore the effect of the measured samples infill on the permittivity measurement. In this work, these topics are further expanded upon.

In section II the microstructure of a 3D printed CF20 sample is examined via optical imaging. CF20 is shown to have an aligned microstructure and expectations about the permittivity of this microstructure are presented. In section III the permittivity of the microstructure is determined using a capacitive measurement technique, and simulations are provided to demonstrate the validity of this measurement method. In section IV the permittivity values of two CF20 samples with differing infill structures are simulated using the tensor obtained in section III and compared to the measured values for the samples. An error of less than 12% is observed between the simulated and measured permittivity values validating the claims presented herein. In section V the conclusions of this work are discussed along with topics of future work for the authors.

II. CF20 MICROSTRUCTURE EXAMINATION

To investigate the underlying cause of the anisotropy, optical imaging was used to examine the microstructure of a CF20 sample. For this, a 10 mm^3 cubic CF20 sample was first printed using 100% infill, 0.2 mm layer height, and one perimeter shell. The sample was then cast in resin, bisected along the XY plane of the sample, and polished to a mirror finish using a 20 nm polishing compound. The polished

---

This work is supported in part by the National Science Foundation under Grant No. IIP-1916535 and IIP-1440110.

sample was then imaged at two locations, the center and the corner of the sample, using a Nikon Eclipse MA100N inverted microscope. Fig. 1 and 2 show the images of the center and corner of the sample respectively. Both images were taken with 250x magnification and have the direction of travel for the 3D printer's nozzle, i.e., the print direction, indicated by the superimposed arrow.

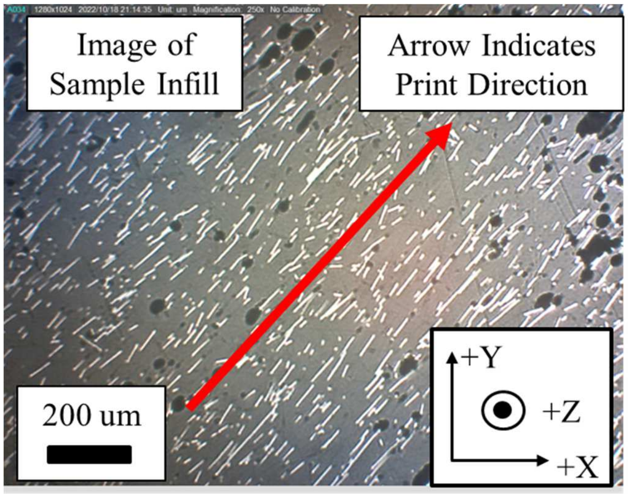

Fig. 1. Image of the CF20 sample corresponding to the center of the sample where the arrow indicates the print direction. Notice how the inclusions are all aligned with this print direction.

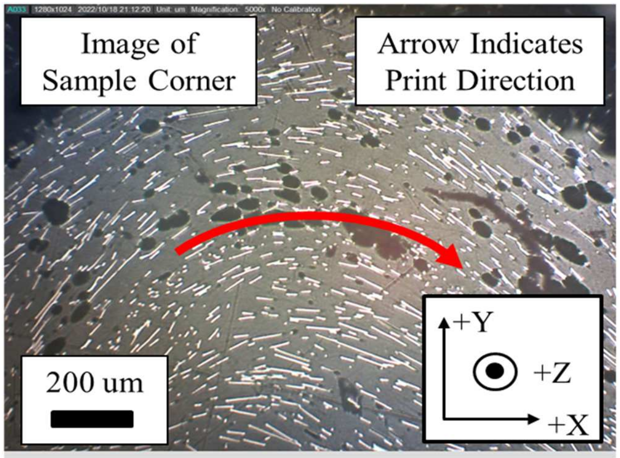

Fig. 2. Image of the CF20 sample corresponding to the corner of the sample where the arrow indicates the print direction. Notice how the inclusions all follow the print direction as the corner of the sample is printed.

As shown in Fig. 2 nearly all of the chopped carbon fiber inclusions are aligned with the print direction and have relatively small off-axis skew. This alignment of the inclusions with the print direction is especially apparent in Fig. 3. where the inclusions alignment follows the 3D printer's print direction as it is printing the corner of the sample. The reason the inclusions are aligned with the print direction, as opposed to being randomly oriented, is due to the mechanics of the 3D printing process.

When the CF20 filament is created, a mixture of randomly aligned inclusions and base material is heated and extruded through a nozzle to create the filament. During printing, this filament enters the 3D printer's nozzle for heating and extrusion where the nozzle diameter narrows from the initial filament diameter (typically 1.8 mm) to the final extrusion diameter (typically 0.4 mm or 0.6 mm). This narrowing, both in the creation and printing of the CF20 filament, creates a funneling effect that aligns the inclusions. Further, when the printer deposits a new layer of material, the nozzle is dragged along the previously deposited material effectively "smearing" the new material in the direction of the print. This combination of funneling and smearing causes the inclusions to become aligned with the print direction as shown in Fig. 1 and Fig. 2.

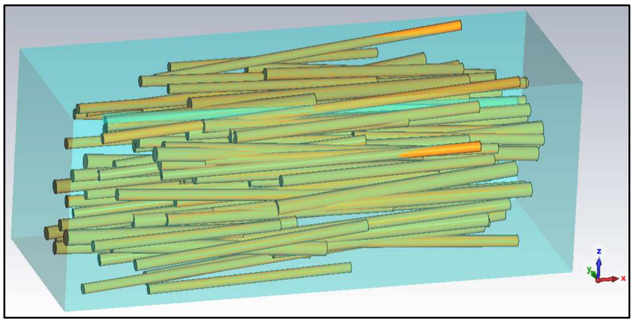

Fig. 3. Rendering of the CF20 Microstructure where the blue material represents the bulk material, and the yellow represents the carbon fiber inclusions.

In Fig. 3 the supposed microstructure of CF20 is presented in 3D for the case where the print direction is aligned with the X axis. This microstructure consists of a bulk material, ColorFabb XT (shown in blue), with carbon fiber inclusions (shown in yellow) that are predominantly aligned with the print direction, have minimal off-axis skew, and have equal semi-axis along the Y and Z axis of the microstructure with a much larger semi-axis along the X axis of the microstructure.

As described in [13] and [14] dielectric mixtures containing conducting nanorods can be modeled using generalizations of the Maxwell Garnett (MG) mixing rule. Using these models, the permittivity of the microstructure shown in Fig. 3 could be analytically calculated. Another possibility to determine the effective dielectric properties of the composite is to perform the full-wave simulation of the geometry in Fig. 3. Unfortunately, both methods cannot be used in practice for two reasons. First, the material properties of the inclusions are a trade secret of the manufacturer and are not available for that reason. Secondly, the 3D geometry of the inclusions cannot be accurately determined from the cross-sections. For example, when the CF20 sample is printed, the microscopic rotation of the inclusions relative to the cross-section plane is not controllable as illustrated in Fig. 4. Because of this uncontrollable rotation of the inclusion, some inclusions are unintentionally cut by the cross-section plane yielding inclusions that are artificially shortened by the imaging process.

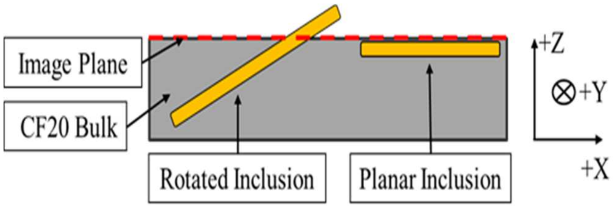

Fig. 4. Diagram of the CF20 sample when imaged, showing the uncontrollable microscopic rotation of the inclusions with respect to the imaging plane and how this can lead to inclusions that are artificially shortened.

Figure 5 shows a high magnification (2500x) image of the inclusions further illustrating this rotated inclusion cutting phenomenon. Notice in Fig. 5 that some of the inclusions appear to penetrate the image plane due to the rotation and have an oval shape at the ends where the inclusion was cut. Because of these effects, both the volume fraction and the length of the inclusion cannot be accurately estimated making use of the generalized MG mixing rules or 3D simulation for calculating the permittivity of the microstructure in Fig. 3. problematic.

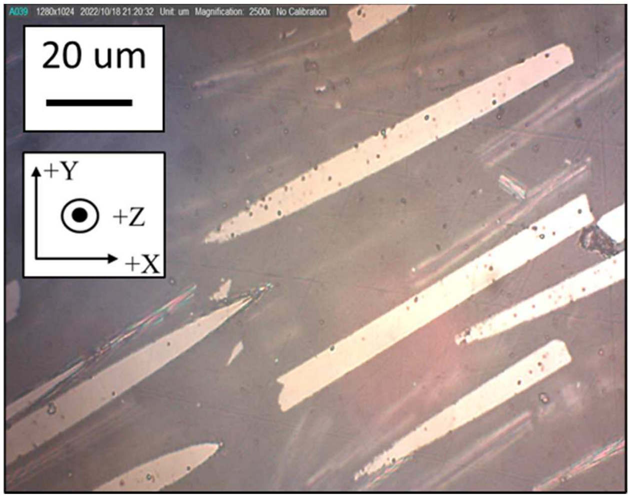

Fig. 5. Image of the CF20 sample at 2500x magnification showing inclusions cut by the imaging plane.

However, instead of calculating the effective permittivity based on the microstructure of the material, it can be directly measured as discussed further in Section III.

Even though the authors lack information to calculate the permittivity of the microstructure, some theoretical expectations about the behavior of the microstructure's permittivity tensor can still be made. As discussed in [15] each inclusion in the microstructure (Fig. 3) can be represented by a prolate ellipsoid that bounds the inclusion. Because of the ellipsoid's broken geometrical symmetry, the dipole moment, polarizability, and importantly the permittivity of the ellipsoid is dependent upon the direction of the electric field that excites the ellipsoid [15]. Noting this, it is theoretically expected that the microstructure of CF20 will lead to a strongly anisotropic permittivity of the material. Moreover, because the ellipsoids that bound the inclusions have an equal semi-axis along the Y and Z axis and a much larger semi-axis along the X axis (for the coordinate system in Fig. 3 and 4) it is also expected that the material have similar values for the Y and Z component of the permittivity tensor and a much larger value for the X component.

III. CF20 MICROSTRUCTURE PERMITVITY MEASUREMENT

To measure the permittivity of the CF20 microstructure a 10 mm^3 cubic CF20 sample was first printed using 100% infill, 0.2 mm layer height, an aligned rectilinear infill, and no perimeter shells. The infill pattern is shown in Fig. 6. The print direction for this infill was aligned with the X axis and the same infill pattern was used for each layer such that the inclusions are predominantly oriented in the X direction in the entire volume of the sample.

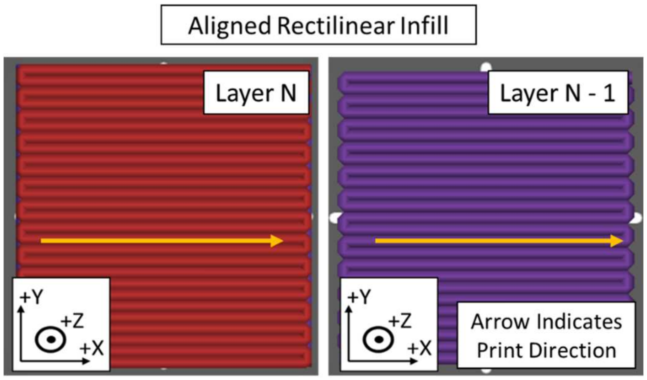

Fig. 6. Rendering of the aligned rectangular infill used for each layer of the printed sample. The print direction was aligned with the X axis of the sample resulting in a sample that was identic to the microstructure shown in Fig. 3.

The sample was placed between two 10 mm x 10 mm copper plates (made of copper tape) creating a parallel plate capacitor. The capacitance of this capacitor was then measured using an LCR meter at 100 kHz and the effective permittivity of the sample was calculated using the parallel plate capacitor formula (the fringing field is ignored):

$$\varepsilon_r = \frac{CD}{\varepsilon_0 A} \qquad (1)$$

where C is the measured capacitance, D is the distance between the plates (10 mm), A is the plate area (100 mm^2), and ε_0 is the vacuum permittivity ($8.85\cdot10^{-12}$ F$\cdot$m^{-1}). This measurement was then repeated for each axis of the sample and a permittivity tensor of $\varepsilon_{r,xyz}$ = (41.1, 4.6, 6.4) was obtained. This tensor agrees with the theoretical expectations of anisotropy presented in section II and is likely correct however further validation is needed (see section IV).

In (1) the fringing fields are assumed to be relatively weak in comparison to the fields between the plates of the high permittivity capacitor and as such can be neglected. To verify this assumption, the LCR measurement technique was simulated in CST Studio Suite. For this simulation a 10 mm^3 sample was placed between two PEC plates and the admittance of the sample was calculated at 100 kHz using a low frequency electro quasistatic solver and open boundary conditions with an additional 10 mm of free space on each side of the model to allow for the fringing field. The capacitance of the sample was then calculated using:

$$C = \frac{Y}{j\omega} \tag{2}$$

where Y is the admittance of the simulated sample at 100 kHz. The permittivity of the simulated sample was then calculated using the capacitance value from (2) and the parallel plate approximation in (1). The actual and calculated permittivity tensors for several samples, as well as relative errors for each component, are given in Table 1.

TABLE I. ACTUAL AND CALCULATED PERMITTIVITY VALUES OBTAINED IN THE SIMULATED EXPERIMENT

Actual Permittivity Tensor ($\varepsilon_X, \varepsilon_Y, \varepsilon_Z$)	Calculated Permittivity Tensor ($\varepsilon_X, \varepsilon_Y, \varepsilon_Z$)	Relative error, %
(1, 1, 1)	(1.53, 1.53, 1.53)	(53, 53, 53)
(5, 5, 5)	(5.5, 5.5, 5.5)	(10, 10, 10)
(40, 40, 40)	(40.5, 40.5, 40.5)	(1.2, 1.2, 1.2)
(20, 20, 7)	(20.5, 20.5, 7.5)	(2.4, 2.4, 7.1)
(40, 5, 5)	(40.5, 5.5, 5.5)	(1.2, 10, 10)

As can be seen for low permittivity values ($\varepsilon_r < 2$) the fringing fields are not weak in comparison to the fields between the plates, as such neglecting these fields yields a substantial error (up to 53% for the air-filled capacitor). However, for modestly large permittivity values ($\varepsilon_r > 5$) the fringing fields are relatively weak, and the error does not exceed 10%, which was deemed acceptable for practical applications.

IV. PERMITTIVITY TENSOR SIMULATION

To validate the permittivity tensor measured in section III the measured permittivity tensors of two CF20 samples were compared to the simulated values. In addition to the sample in section III with the parallel infill (Fig. 6) a sample with the orthogonal infill was printed (Fig. 7). For the orthogonal infill the print direction in the layers is ±45 degrees relative to the X axis, such that the angle between the infill lines in the adjacent layers is 90 degrees. The permittivity tensors for the orthogonal infill sample were measured using the same procedure as for the parallel infill sample in section III.

Both samples were simulated in full-wave (CST low-frequency electro quasistatic solver) using the modes presented in Fig. 8. The models recreated the infill structure of the samples where each infill line was represented by a dielectric parallelepiped. The layers in the models were created using two different materials (orange and green in Fig. 8). For the parallel infill model, the materials had a permittivity tensor $\varepsilon_{r,xyz}$ = (41.1, 4.6, 6.4) as measured in sec. III. For the orthogonal infill model, however, the permittivity tensor was set to $\varepsilon_{r,xyz}$ = (41.1, 4.6, 6.4) for the green material and to $\varepsilon_{r,xyz}$ = (4.6, 41.1, 6.4) to reflect the change in the print direction. For simplicity of model generation, the print directions were aligned with the X and Y axes as opposed to the 45-degree alignment of the print direction in the actual sample.

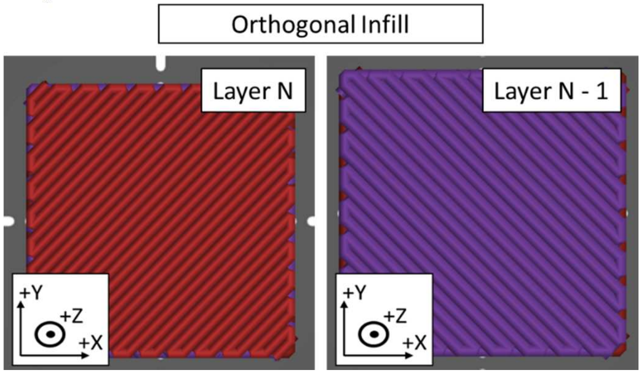

Fig. 7. The orthogonal (rectilinear) infill used for sample 2 for layer N and N – 1. Notice how for layers N and N – 1 the print direction rotates 90 degrees around the Z axis creating adjacent layers that are orthogonal.

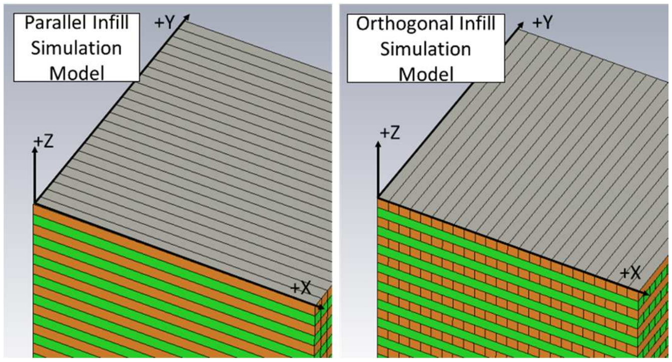

Fig. 8. Simulation models for the parallel and orthogonal infills. Notice how each layer is aligned with the X axis of the sample in the parallel infill model (right). and how green layers are aligned with the X axis and orange layers are aligned with the Y axis in the orthogonal infill model (left). The results of the simulation along with the measured values are given in Table II.

TABLE II. COMPARISON OF SAMPLE PERMITTIVITY MEASUREMENTS TO SIMULATION

	X – Axis		Y – Axis		Z – Axis	
	Meas.	Sim.	Meas.	Sim.	Meas.	Sim.
Parallel Infill Sample	41.1	41.6	5.5	5.1	6.4	6.8
Orthogonal Infill Sample	21.2	23.9	19.6	22.1	6.8	6.8

The difference between the simulated and measured permittivity values for each sample did not exceed 12%. This can be considered acceptable for many practical applications and indicates a good agreement between the simulation and measurement results, validating the claim that the permittivity tensor of CF20 is close to $\varepsilon_{r,xyz}$ = (41.1, 4.6, 6.4).

Further, the results presented in Table II also illustrate the profound effect of the infill on the permittivity values. For the parallel infill sample, the permittivity reaches a value of 40 in the direction of the infill lines and is significantly lower in the other two directions, whereas for the orthogonal infill sample, the permittivity is equal in the X and Y directions (i.e., in the layer plane) and its value is reduced by half relative to the maximum value for the parallel infill sample.

V. CONCLUSION

In this work, the permittivity of CF20 was further examined. By optically imaging a 3D printed CF20 sample it was determined that the material contains elongated carbon fiber inclusions which are predominantly aligned with the print direction. The measurement and simulation results of this aligned microstructure both agree with the theoretical expectations of anisotropy allowing one to conclude that this aligned microstructure is the reason for the strong anisotropy reported in this work and previously in [12]. Further, the infill of the sample was shown to have a strong influence on the effective permittivity tensor of the sample, leading to the pronounced difference in permittivity values observed for the two samples in section IV.

Moreover, in [12] CF20 was reported to have a permittivity tensor of $\epsilon_{r,xyz}$ = (21.2, 19.6, 6.8). While this is the correct tensor for the sample studied in [12] it is not the correct permittivity tensor for the material itself. In [12] the authors did not consider the influence of the infill on the permittivity measurements when reporting the tensor for CF20 leading to an erroneous reporting of the CF20 permittivity tensor. As shown in this work the correct permittivity tensor of CF20 is likely to be $\varepsilon_{r,xyz}$ = (41.1, 4.6, 6.3).

Lastly, the strong influence of the infill on the effective permittivity tensor of a sample gives rise to the idea that one could intentionally modulate the macrostructure of a sample, i.e. its infill, to achieve a desired permittivity tensor when using anisotropic materials. Considering the accuracy of the simulations performed in this work it is likely that one could design the required macrostructure to achieve a given tensor. This is a topic of future work for the authors.

REFERENCES

[1] S. Desai and J. Njuguna, “Enhancement of thermal conductivity of materials using different forms of natural graphite,” *IOP Conference Series: Materials Science and Engineering*, vol. 40, p. 012017, 2012.

[2] “Stain and Chemical Resistance,” *Stain and chemical resistance*. [Online]. Available: https://hpp.arkema.com/en/product-families/orgasol-specialty-polyamide-powders/stain-and-chemical-resistance/. [Accessed: 01-Jan-2023].

[3] J. P. Diebold and S. Czernik, “Additives to lower and stabilize the viscosity of pyrolysis oils during storage,” *Energy & Fuels*, vol. 11, no. 5, pp. 1081–1091, 1997.

[4] “Conductive PLA,” *pasta*. [Online]. Available: https://www.proto-pasta.com/pages/conductive-pla. [Accessed: 23-Dec-2022].

[5] “Glowfill,” Home page. [Online]. Available: https://colorfabb.com/glowfill. [Accessed: 23-Dec-2022].

[6] “Tough pla black,” *Home page*. [Online]. Available: https://colorfabb.com/tough-pla-black. [Accessed: 23-Dec-2022].

[7] “XT-CF20,” *Home page*. [Online]. Available: https://colorfabb.com/xt-cf20. [Accessed: 23-Dec-2022].

[8] R. Reese et al., "Fully Dielectric Rod Antenna Arrays with High Permittivity Materials," 2019 12th German Microwave Conference (GeMiC), 2019, pp. 13-16, doi: 10.23919/GEMIC.2019.8698141.

[9] C. Ding and K. -M. Luk, "Low-Profile Planar Dielectric Polarizer Using High-Dielectric-Constant Material and Anisotropic Antireflection Layers," in IEEE Transactions on Antennas and Propagation, vol. 69, no. 12, pp. 8494-8502, Dec. 2021, doi: 10.1109/TAP.2021.3090847.

[10] P. H. Zapata-Cano, E. Vandelle, T. Q. van Hoang and B. Loiseaux, "Microwave Absorber Made of Hanoi-Tower Shaped Dielectric Resonators and a Magnetic Support," 2022 16th European Conference on Antennas and Propagation (EuCAP), Madrid, Spain, 2022, pp. 1-5, doi: 10.23919/EuCAP53622.2022.9769354.

[11] T. Fujita et al., "Alternate lamination of high-permittivity dielectric materials for super thin wave absorber," 2012 42nd European Microwave Conference, 2012, pp. 1166-1169, doi: 10.23919/EuMC.2012.6459384.

[12] A. Harmon, V. Khilkevich and K. M. Donnell, "High Permittivity Anisotropic 3D Printed Material" 2022 IEEE International Symposium on Electromagnetic Compatibility & Signal/Power Integrity (EMCSI), 2022, pp. 1-6, doi: 10.1109/EMCSI39492.2022.9889552.

[13] M. Y. Koledintseva, S. K. Chandra, R. E. DuBroff, and R. W. Schwartz, “Modeling of dielectric mixtures containing conducting inclusions with statistically distributed aspect ratio,” *Progress In Electromagnetics Research*, vol. 66, pp. 213–228, 2006.

[14] M. Y. Koledintseva, R. E. DuBroff, and R. W. Schwartz, “Maxwell Garnett rule for dielectric mixtures with statistically distributed orientations of inclusions,” *Progress In Electromagnetics Research*, vol. 99, pp. 131–148, 2009.

[15] A. H. Sihvola, *Electromagnetic mixing formulas and applications*. London: Institution of Electrical Engineers, 2008.